Supplementary Information (SI) for Journal of Materials Chemistry A.

Supporting Information

Ionic-liquid Engineered Interfacial π-π anchored Cobalt dispersed N, F, B- doped Carbon matrix as an Oxygen Electrocatalyst for Advanced Zinc-Air Battery

Nadar Allwyn[a,b], Mukkattu Kuniyil Nikhil Chandran[a,b], Venkatraman Maithreyan[a #], Maria Antony Shalom[a #], and Marappan Sathish[a,b]*

[a] Electrochemical Power Sources Division, CSIR-CECRI, Karaikudi-630 003, Tamil Nadu, India.

[b] Academy of Scientific and Innovative Research (AcSIR), Ghaziabad- 201002, India

† Electronic supplementary information (ESI) available.

[#] Authors with equal contribution

Corresponding Author

*E-mail: msathish@cecri.res.in

Material Characterization

To investigate and illustrate the characteristics of the synthesized electrocatalyst, several analytical techniques have been employed. A Rigaku X-ray diffractometer working with Cu k radiation at a wavelength of 1.541 Å was used to examine the crystalline details of the generated catalyst. The nitrogen adsorption-desorption isotherm was found using Quantachrome® ASiQwinTM in order to get the exact surface area. To determine the types and levels of defects present in the annealed counterpart, Raman spectroscopy (LabRAM HR Evolution, Horiba) was employed. The composites' morphology and microstructure were investigated using a field emission scanning electron microscope (FE-SEM; Carl Zeiss, AG SUPRA 55VP). The particle size and the distribution of elements of the composite was examined using high-resolution transmission electron microscopy (HR-TEM) analysis (Talos F200S [FEI] with a field emission gun), using Cu grid as the substrate and the drop cast method to cover the sample. Using an X-ray photoelectron spectrometer (ESCALAB 250 Xi) from Thermo Scientific, the chemical composition and degree of oxidation were determined. Fourier transform infrared spectroscopy (FT-IR) was used to analyse the functional groups that were present in the electrocatalyst.

Methodological approach for the oxygen electrocatalysis

Utilizing a rotating electrode design with a rotator in a standard three-electrode setup, the electrochemical ORR performance was assessed using the Biologic VSP 300 potentiostat and PINE instrument. The working electrode was made up of a 5 mm-diameter rotating disc electrode (RDE) made of glassy carbon (GC), an Ag/AgCl reference electrode that contained 3 M KCl, and a 1 cm^2 platinum foil counter electrode. For the purpose of achieving a homogeneous dispersion for the catalytic ink for ORR, about 5 mg of the active component is dispersed using ultrasonic for 45 min in a volume ratio of 60:30:10 with water, isopropanol, and 5 weight percent Nafion binder. The catalytic ink was drop cast over the working electrode in about 15 μL, yielding an overall loading of 0.25 mg/cm^2. Prior to usage, the GC electrode was let to air dry for 5 h. A comparable treatment with the same mass loading was given to Pt/C, the ORR benchmark standard catalyst. With a scan rate of 10 mV/s and a potential window of 1 to 0.2 V vs. RHE at room temperature, the ORR activity was measured using linear sweep voltammetry (LSV) in 0.1 M KOH electrolyte at various rpms between 100 and 2025 rpm. Before the experiment, the electrochemical setup was sufficiently purged with nitrogen gas to remove oxygen for 45 minutes. The experiment was then conducted under saturated oxygen, which had also been purged for 30 minutes. Cyclic voltammetry was used to evaluate the electrochemical active surface area (ECSA) of a 0.1 M KOH solution, varying the scan rate from 10 to 100 mV/s. The ECSA was measured within the range of 1.01 to 1.07 V vs. RHE. The following formula was used to determine the ECSA.

$$\mathbf{ECSA = C_{dl}/C_s \times S}$$

Where C_{dl} is the double layer capacitance determined by the slope of plot of current density versus scan rate according to the equation $\Delta \mathbf{J = C_{dl} \times} \boldsymbol{v}$, C_s is the specific capacitance of smooth surface which is 40 µF/cm^2 and S is the geometric surface area of the electrode. Using the formula $E_{Ag/AgCl} + 0.059\ p^H + 0.2 = E_{RHE}$, the reported potential for Ag/AgCl was transformed to a reversible hydrogen electrode (RHE) for comparison with reference values. The half-wave potential for the oxygen reduction process would be represented by the potential measured at the current density of $J_{=3mA/cm^2}$. The electron transfer number, n, is based on a linear relationship between the total measured current, J, and the angular velocity, (rad s^{-1}), whose slope yields n. The Koutecky-Levich (KL) plot, which is based on the equation below, was used to determine n.

$$\mathbf{1/J = 1/(nFC_oD^{2/3}\boldsymbol{v}^{-1/6}) * 1/\omega^{1/2} + 1/J_k}$$

Where F is the Faraday's constant (96480 C mol^{-1}), C is the oxygen concentration in 0.1 M KOH (1.9×10^{-5} cm^2 s^{-1}), v is the kinematic viscosity of the electrolyte (0.01 cm^2 s^{-1}), and J_k is the kinetic current. The slope of the Tafel plot was used to analyse the process kinetics. The Tafel slope was calculated using the formula = b log J + a, where J is the current density in mA/cm^2 and b is the Tafel slope in mV dec-1. An estimate of the electrocatalytic ORR's efficiency may be obtained by combining the onset potential, overpotential at a current density of 3 mA/cm^2, limiting current density (j_d), Tafel slope, and KL plot. Using cyclic voltammetry, the catalyst's stability was assessed for 5000 cycles at a scan rate of 100 mV/s, then to ensure the data collected before cycling could be repeated, LSV measurements were performed again after cycling. The OER activity was also evaluated in the same setup with a 1 M KOH electrolyte, but in the potential range of 1 to 2 V vs. RHE.

Construction and evaluation of zinc-air battery performance

The prototype acrylic sheet-based zinc-air battery was utilized which consist of a zinc foil anode (1 cm^2) with a 0.6 mm thickness, a cathode with a gas diffusion layer (GDL) containing the catalyst, and an electrolyte consisting of 0.2 M zinc acetate and 6 M KOH with air opening of 1 cm^2. In order to get a homogeneous dispersion, 5 mg of the active ingredient was sonicated for 30 minutes in a 60:30:10 volume ratio solution including water, isopropanol (IPA), and nafion binder (5 wt%). To get a loading of 1 mg/cm^2, 200 μL of the catalytic ink was drop cast onto a 1 cm^2 GDL, dried for 5 h at 60 ^{o}C in a hot air oven, and then used as cathode material. Pt/C + RuO_2 was used as the cathode in the construction of a similar zinc-air battery. With the use of sand paper, the zinc foil was thoroughly polished to eliminate any surface imperfections. Polished zinc foil, surface-modified GDL, and an electrolyte solution of 6 M KOH + 0.2 M zinc acetate were used to make the whole cell. For the cathode and anode, respectively, current collectors made of nickel foam and stainless-steel foil were used. To determine if there is any self-discharge that causes voltage loss, the open circuit voltage (OCV) of the built zinc-air battery was evaluated in the potentiostat for a maximum of 15 h. The battery was then polarized between the OCV voltage range and 0.5 V in order to measure the system's peak power density and discharge rate. Furthermore, the device's rate capability was tested by discharging at different current densities ranging from 0.5 to 50 mA/cm^2. This allowed for the evaluation of the device's resistance to that specific current density, which is a necessary condition for any stable battery. The electrical rechargeability test was then conducted, which comprised delivering a constant load of 5 mA/cm^2 for 20 minutes per cycle (10 minutes for charging and 10 minutes for discharging). To assess the high-rate performance, the rechargeability test was tested at a longer charge / discharge timing of 2 h, 4 h, 6 h, 8 h, 10 h, and 144 h per cycle. Then to determine the maximum deliverable capacity of the device, complete discharging was performed at current density of 5 mA/cm^2. The zinc plate was measured both before and after the procedure, and the normalized capacity with regard to weight reduction (specific capacity) was calculated using the following method based on the weight difference.

$$\textit{Specific capacity (in mAh/g}_{Zn}\textit{)} = \textit{(discharge current} \times \textit{discharge time) / Zn consumed}$$

The device's practical application was demonstrated by series-connecting two batteries and utilizing it to illuminate an LED panel. A constant ambient environment was maintained throughout the experiment for all measurements.

Quasi-solid-state flexible zinc-air battery

A zinc-air quasi-solid-state battery was built with a gel electrolyte based on KOH and polyacrylamide (PAM). After dissolving around 3 g of acrylamide in 30 mL of distilled water, 10 mg of N, N methylene bisacrylamide was added as a crosslinking agent, and 50 mg of ammonium persulphate was added as an initiator. The mixture was then stirred for one hour. After the solution was poured into a petri dish, it was incubated at 60 ^{o}C for 6 h to polymerize to PAM. This PAM-based gel electrolyte was then obtained by immersing it in a solution of 6 M KOH and 0.2 M zinc acetate for 72 h. A 1 × 2 cm^2 piece of zinc foil served as the anode, and the catalyst was drop cast over a carbon cloth that had a comparable size serving as the air cathode. A flexible zinc-air battery was made by sandwiching catalyst-coated carbon fabric, gel electrolyte, and zinc foil. Like the liquid electrolyte-based zinc-air battery, the complete discharge and polarization processes were carried out to determine the specific capacity and peak power density, respectively. The charge-discharge experiments were conducted at 2 mA/cm^2 in an analogous manner.

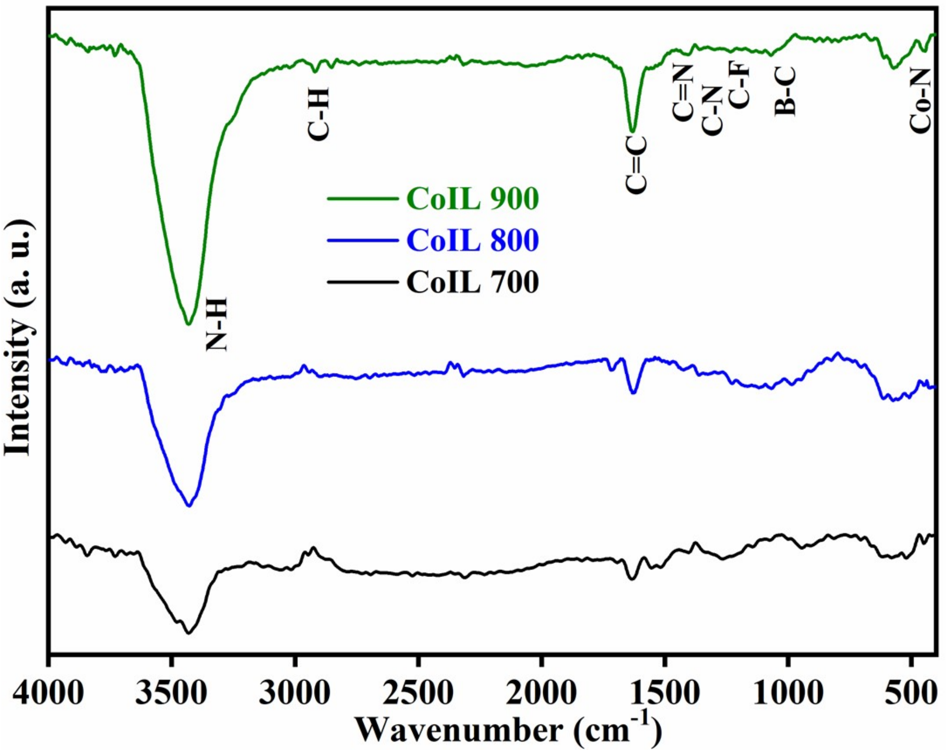

Figure S1. FT-IR spectrum of CoIL 700, CoIL 800, and CoIL 900

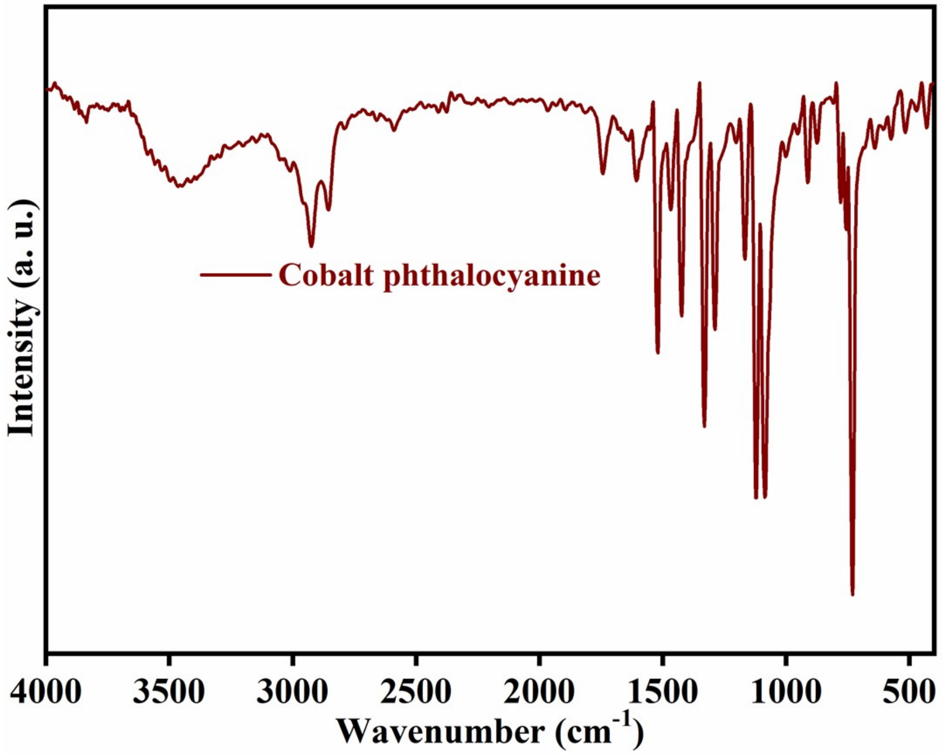

Figure S2. FT-IR spectrum of bare Cobalt phthalocyanine

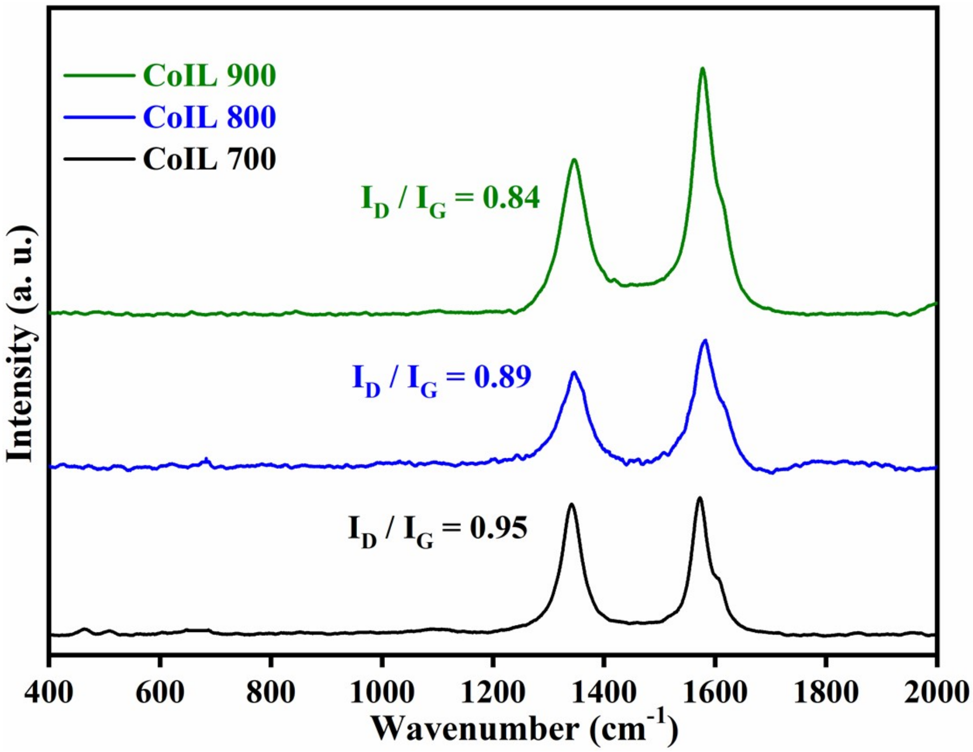

Figure S3. Raman spectrum of CoIL 700, CoIL 800, and CoIL 900

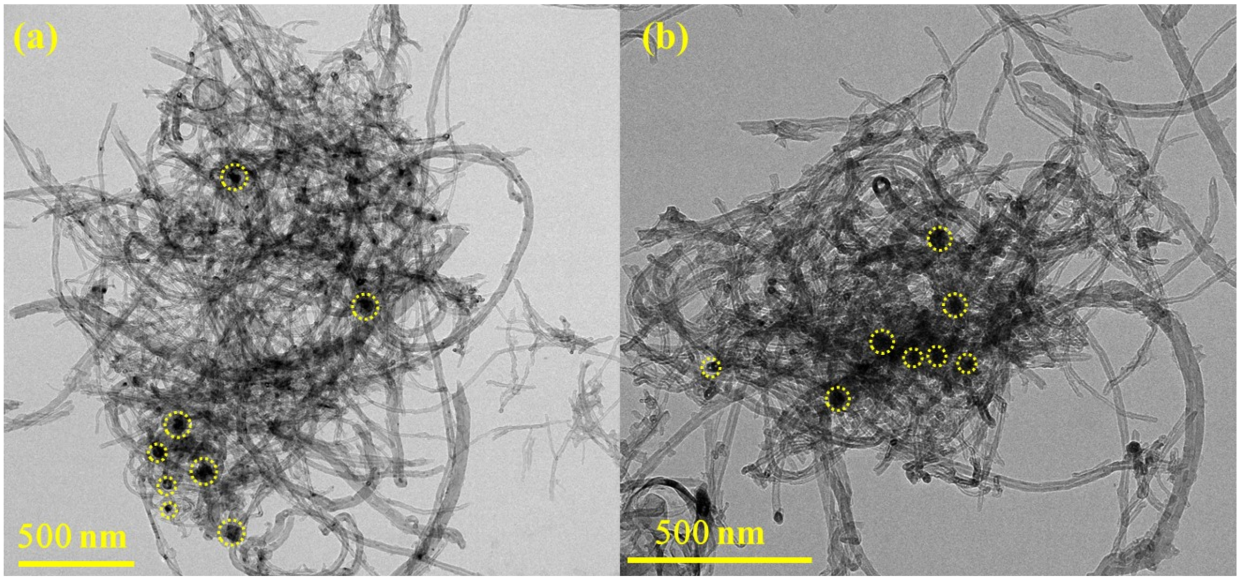

Figure S4. (a-b) HR-TEM images of bare CoIL 700 with the circled ones corresponding to cobalt nanoparticles

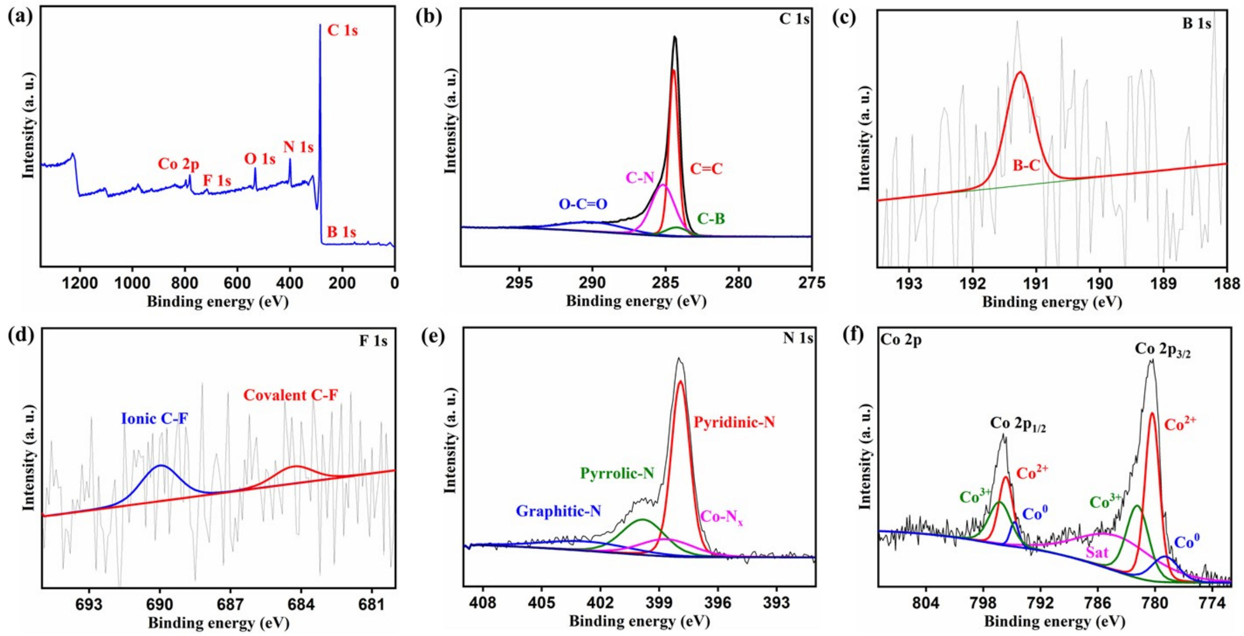

Figure S5. (a) XPS survey spectrum of CoILPh 800, (b) deconvoluted C 1s spectra of CoILPh 800, (c) deconvoluted B 1s spectra of CoILPh 800, (d) deconvoluted F 1s spectra of CoILPh 800, (e) deconvoluted N 1s spectra of CoILPh 800, and (f) deconvoluted Co 2p 1s spectra of CoILPh 800

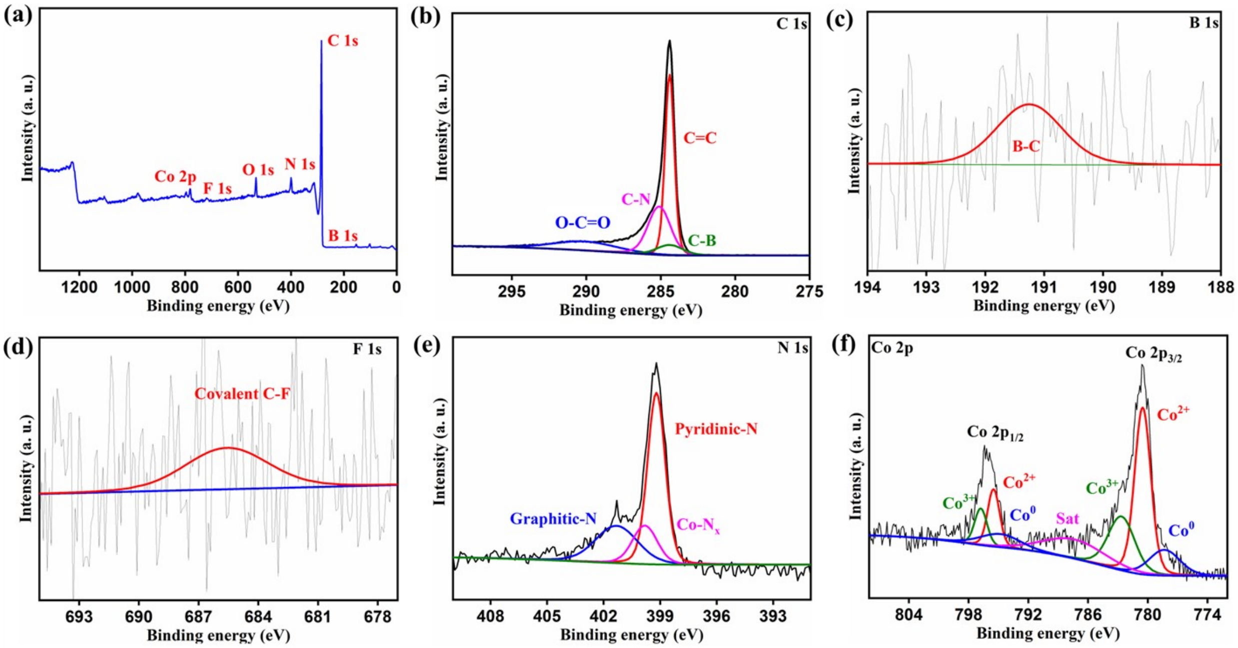

Figure S6. (a) XPS survey spectrum of CoILPh 900, (b) deconvoluted C 1s spectra of CoILPh 900, (c) deconvoluted B 1s spectra of CoILPh 900, (d) deconvoluted F 1s spectra of CoILPh 900, (e) deconvoluted N 1s spectra of CoILPh 900, and (f) deconvoluted Co 2p 1s spectra of CoILPh 900

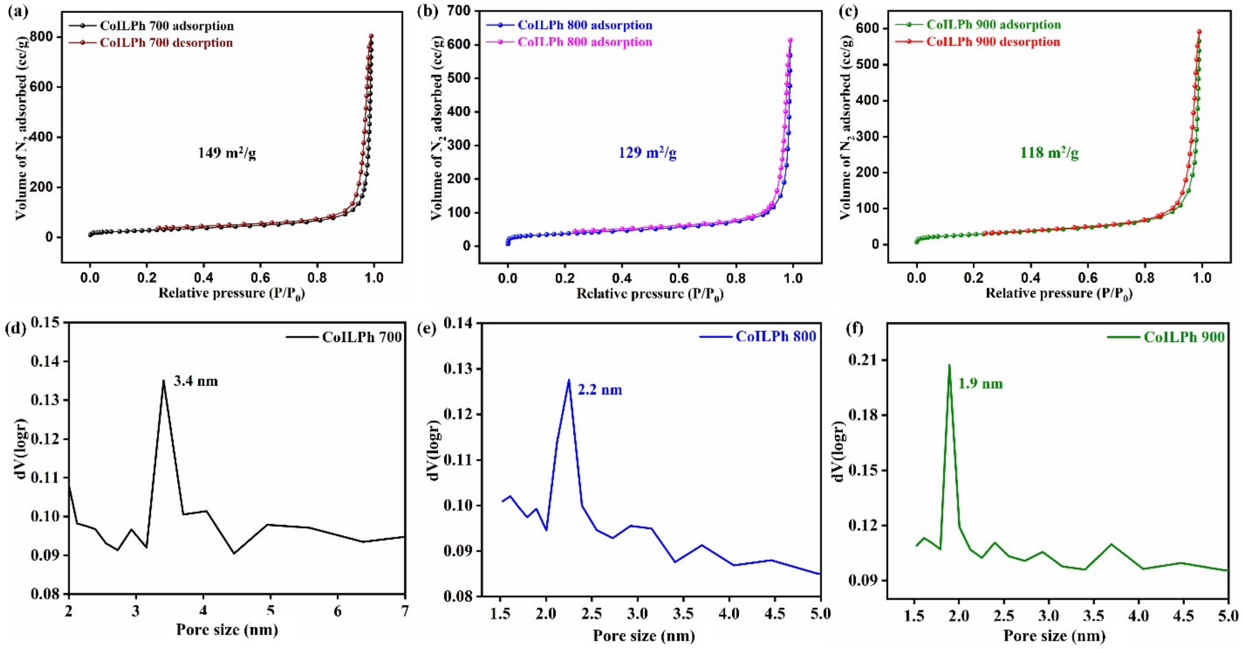

Figure S7. N_2 adsorption-desorption isotherm of CoILPh 700, CoILPh 800, and CoILPh 900 measured at 77 K with its corresponding pore size distribution.

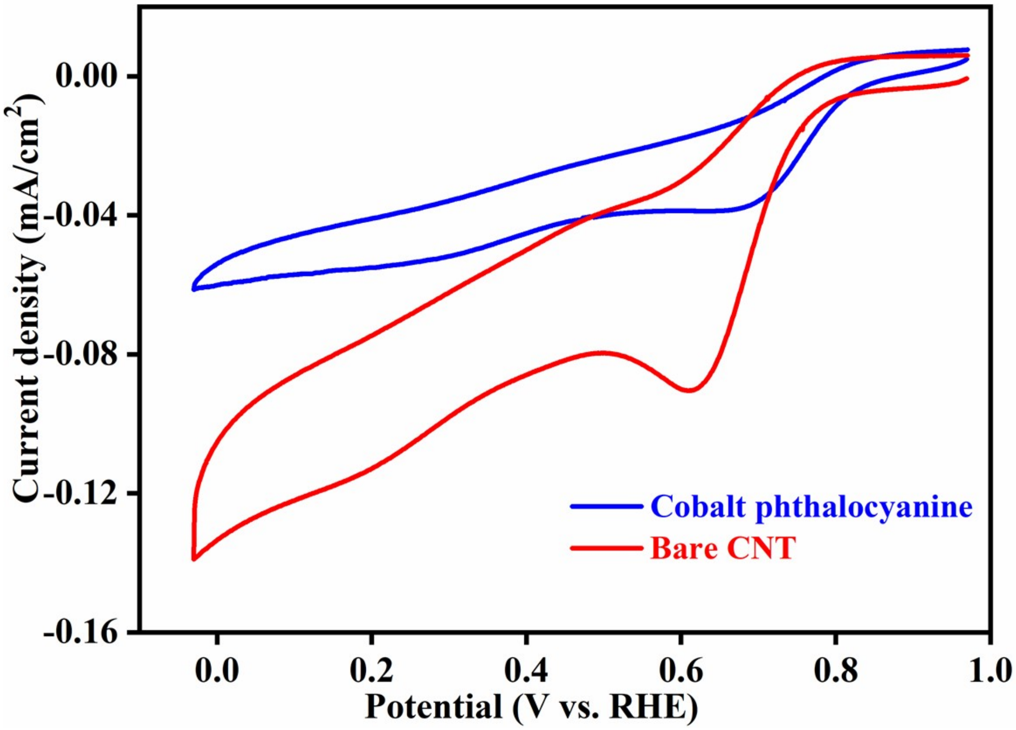

Figure S8. CV plot of cobalt phthalocyanine and bare CNT in 0.1 M KOH at the scan rate of 10 mV/s

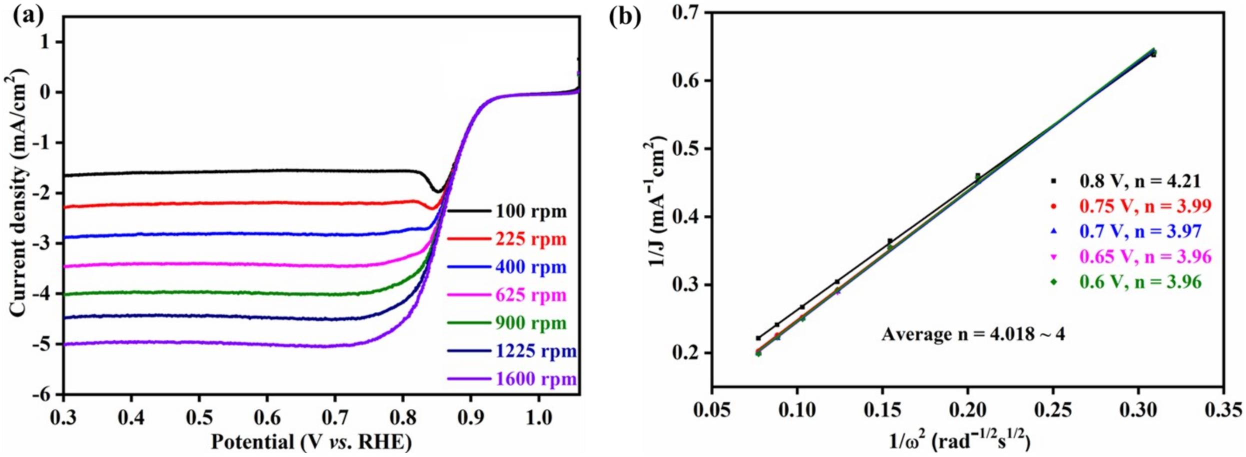

Figure S9. (a) LSV plot of CoIL 700 at various rpm from 100 rpm to 1600 rpm in 0.1 M KOH at the scan rate of 10 mV/s, (b) Koutecky Levich plot of CoIL 700 and the number of electrons transferred

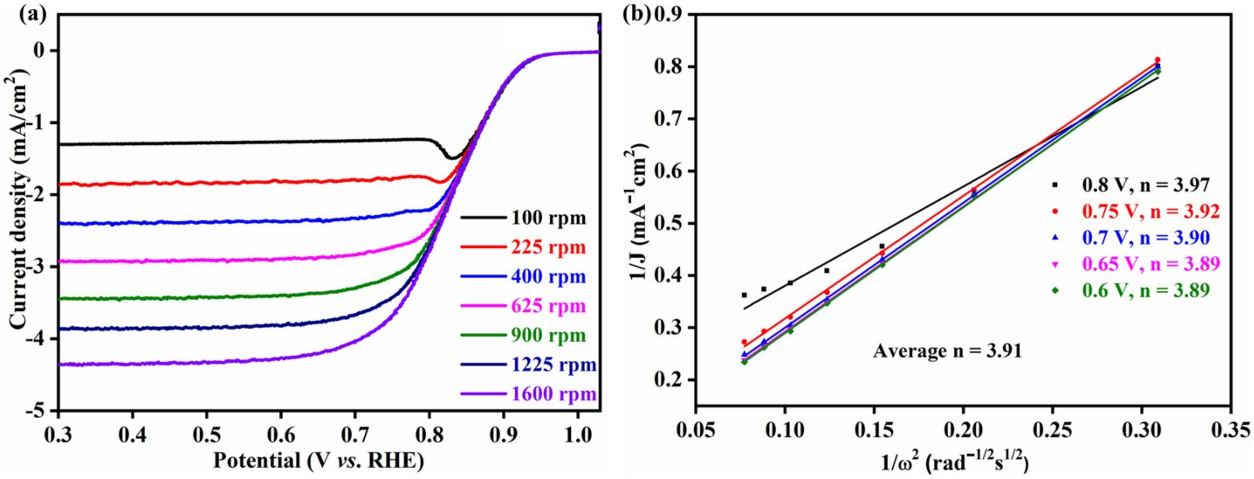

Figure S10. (a) LSV plot of CoIL 800 at various rpm from 100 rpm to 1600 rpm in 0.1 M KOH at the scan rate of 10 mV/s, (b) Koutecky Levich plot of CoIL 800 and the number of electrons transferred

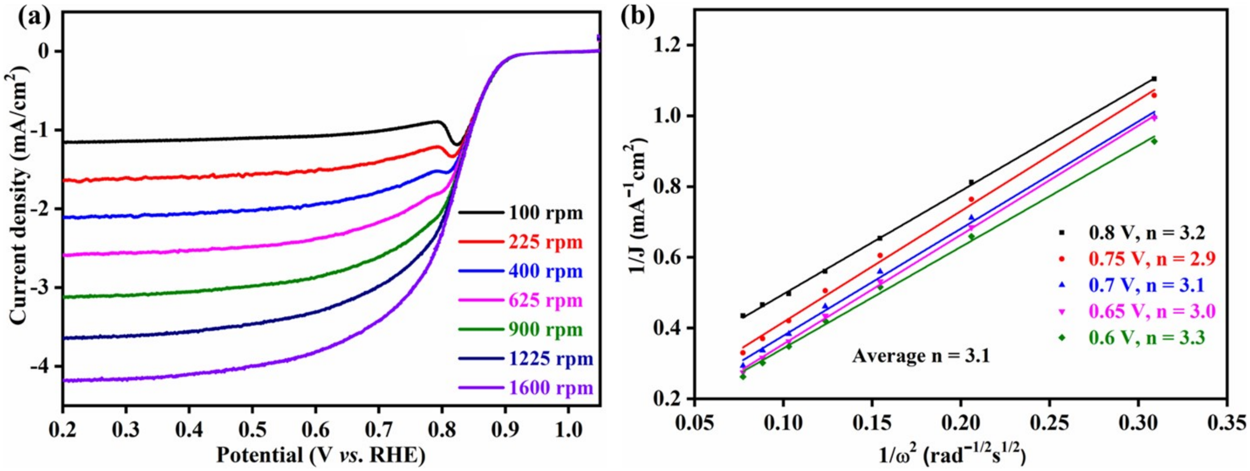

Figure S11. (a) LSV plot of CoIL 900 at various rpm from 100 rpm to 1600 rpm in 0.1 M KOH at the scan rate of 10 mV/s, (b) Koutecky Levich plot of CoIL 900 and the number of electrons transferred

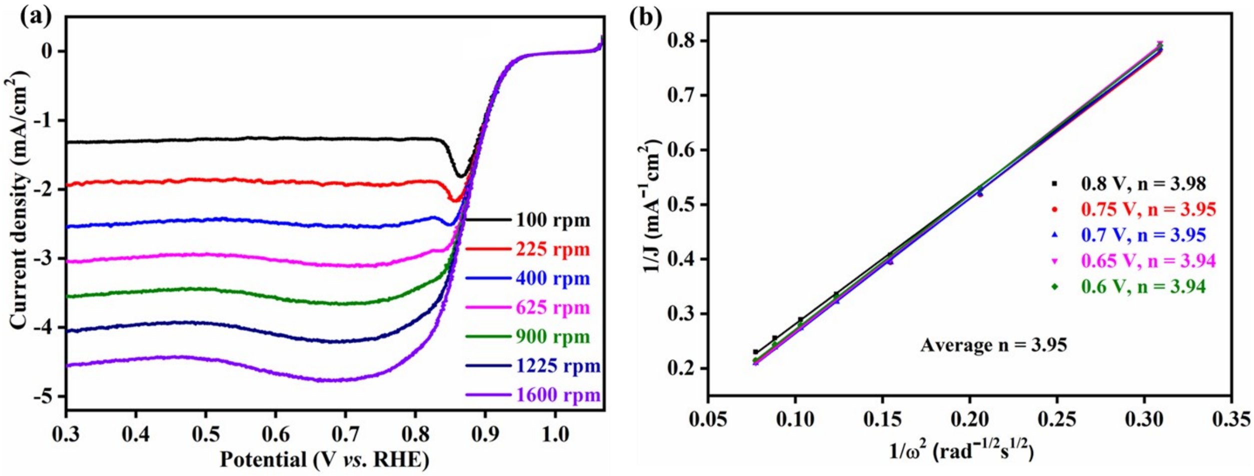

Figure S12. (a) LSV plot of CoILPh 800 at various rpm from 100 rpm to 1600 rpm in 0.1 M KOH at the scan rate of 10 mV/s, (b) Koutecky Levich plot of CoILPh 800 and the number of electrons transferred

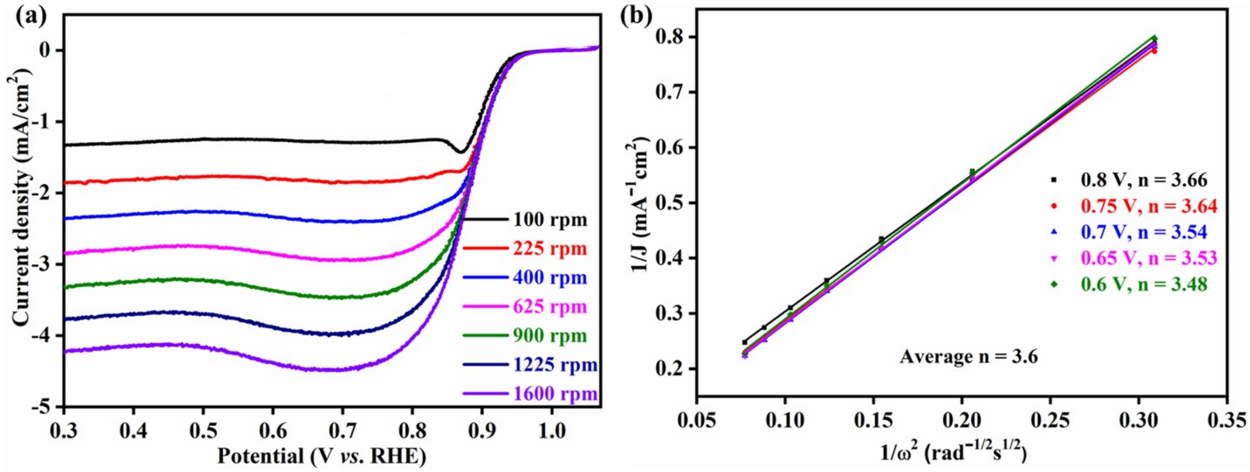

Figure S13. (a) LSV plot of CoILPh 900 at various rpm from 100 rpm to 1600 rpm in 0.1 M KOH at the scan rate of 10 mV/s, (b) Koutecky Levich plot of CoILPh 900 and the number of electrons transferred

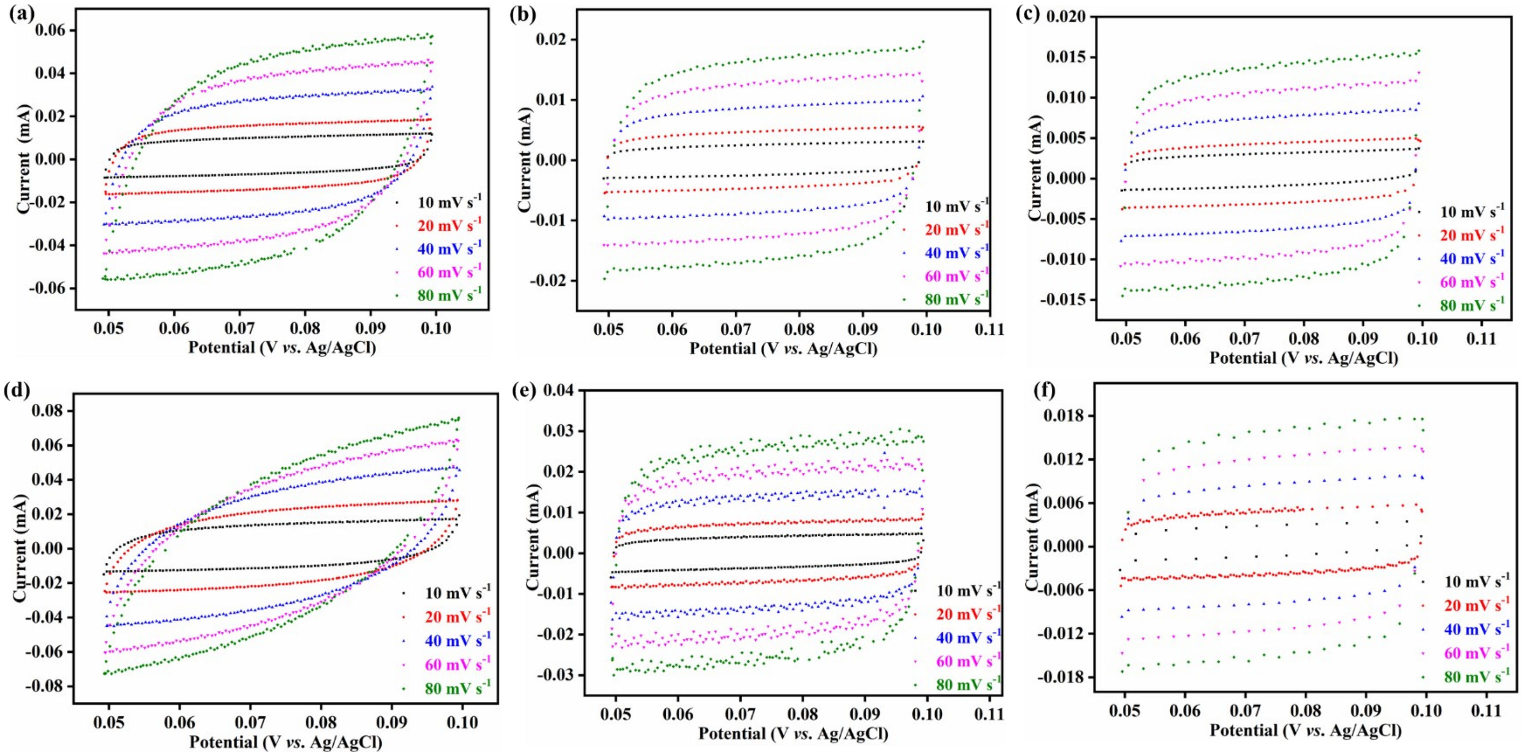

Figure S14. Cyclic voltammogram of (a) CoIL 700, (b) CoIL 800, (c) CoIL 900 (d) CoILPh 700, (e) CoILPh 800, and (f) CoILPh 900 in 0.1 M KOH in the potential window ranging from 0.05 V to 0.10 V *vs*. Ag/AgCl (EDLC region) at varying scan rates of 10, 20, 40, 60, 80 mV/s for the measurement of electrochemical active surface area.

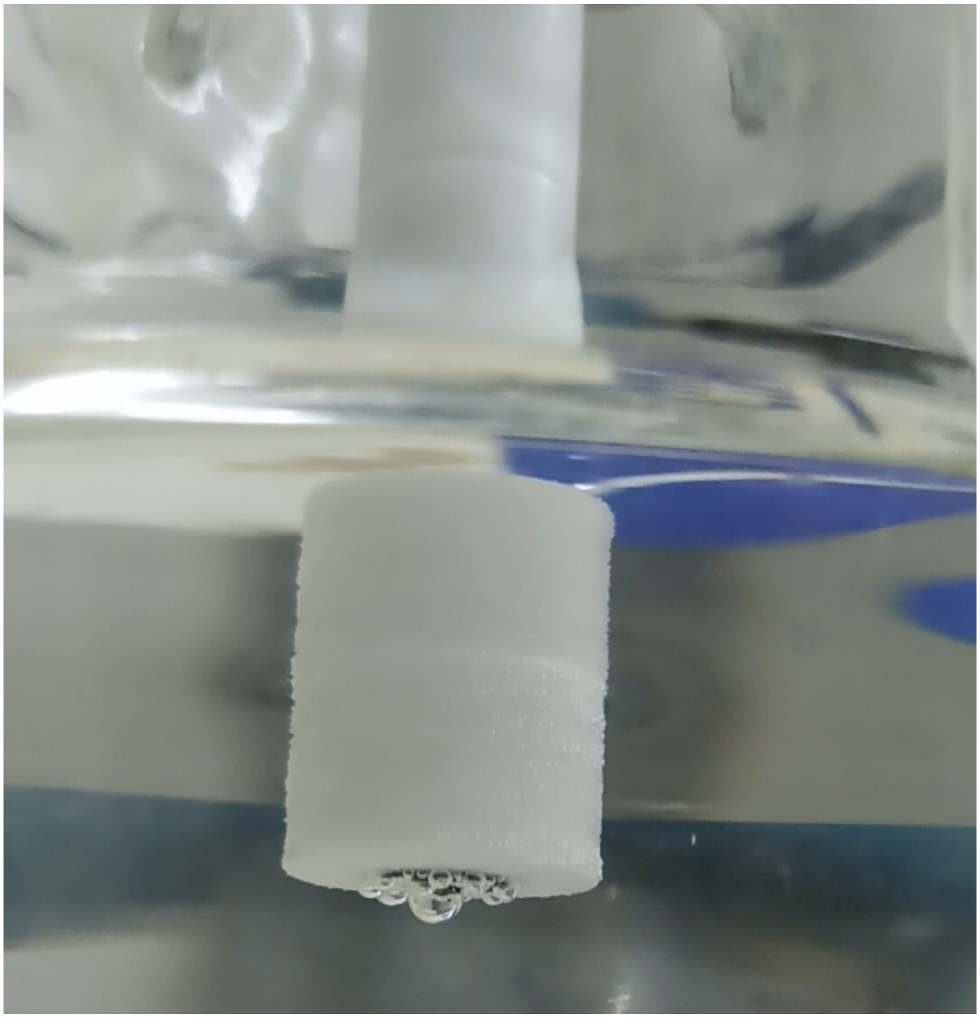

Figure S15. Photograph of glassy carbon electrode after carrying out OER activity for CoILPh 700

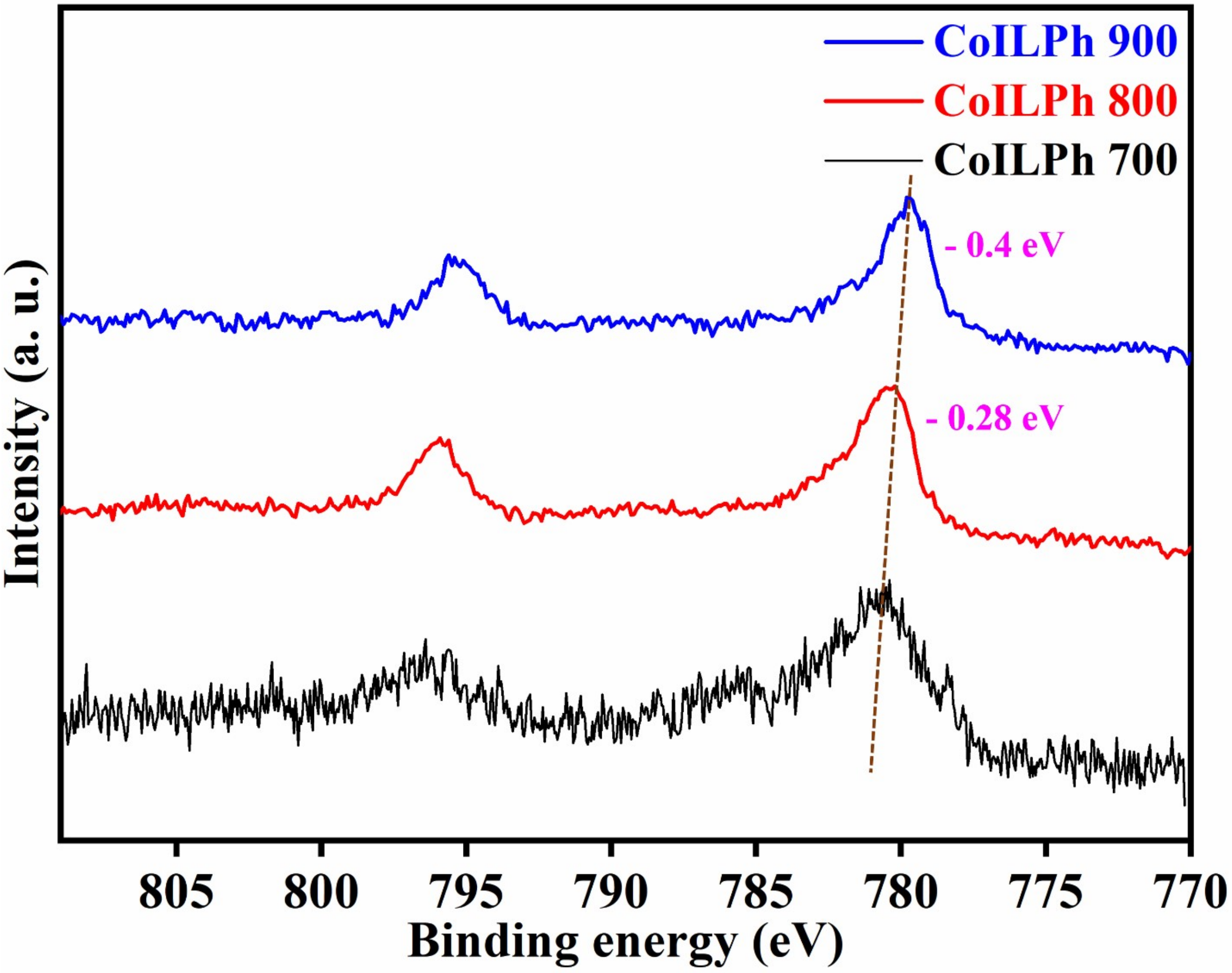

Figure S16. Comparative Co 2p XPS spectrum of CoILPh 700, CoILPh 800, and CoILPh 900

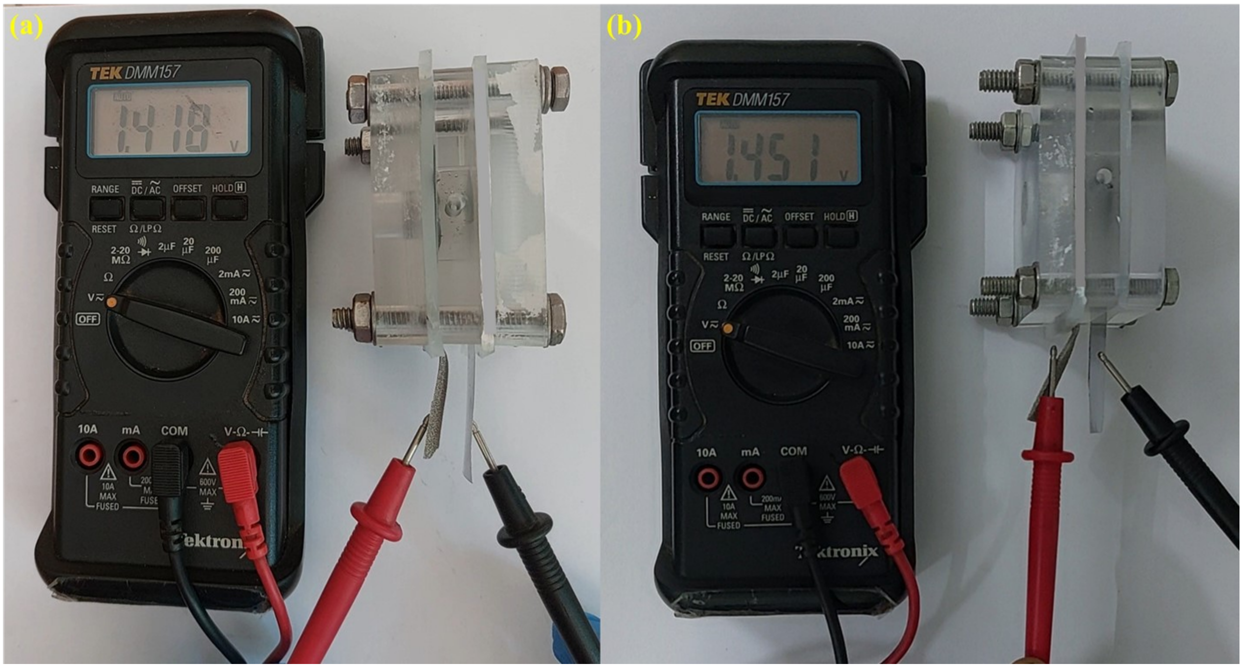

Figure S17. The OCV of as-assembled home-made zinc-air battery based on (a) Pt/C+RuO$_2$, and (b) CoILPh 700 and cathodes

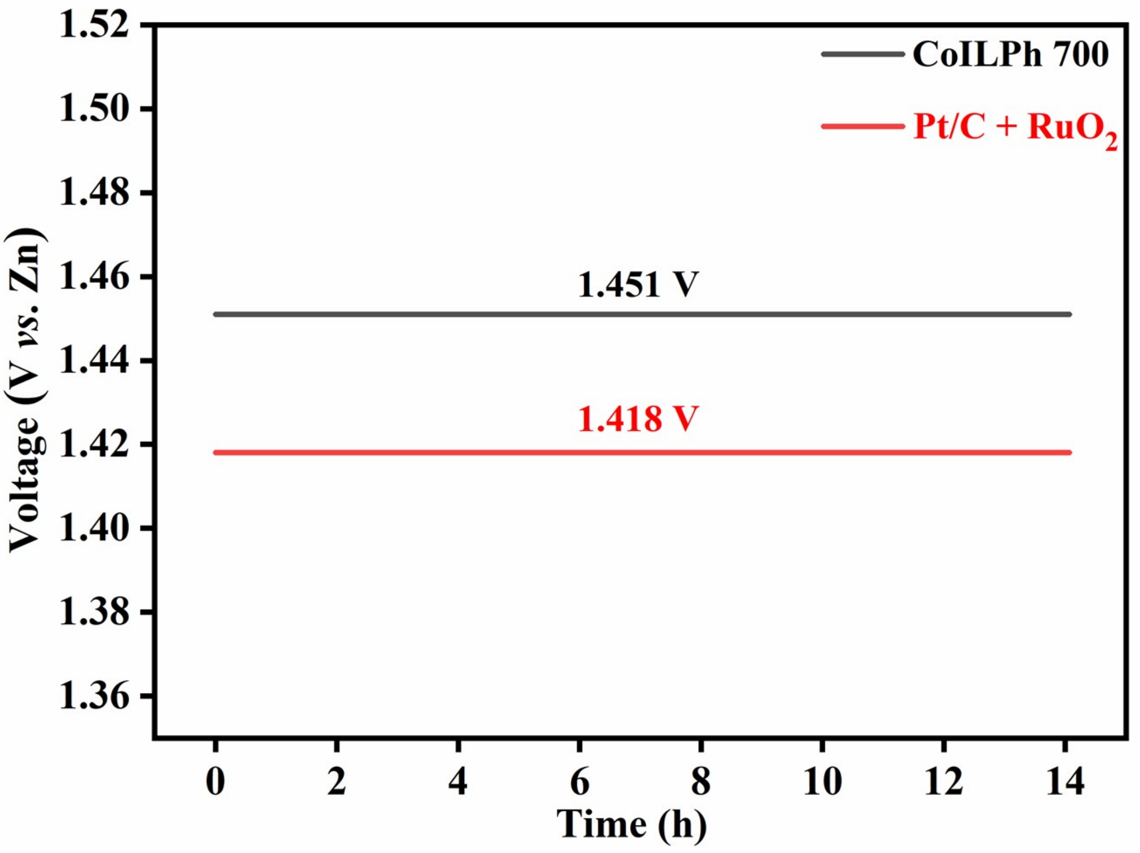

Figure S18. The OCV plot of as-assembled home-made zinc-air battery with CoILPh 700 and Pt/C+RuO_2 cathodes

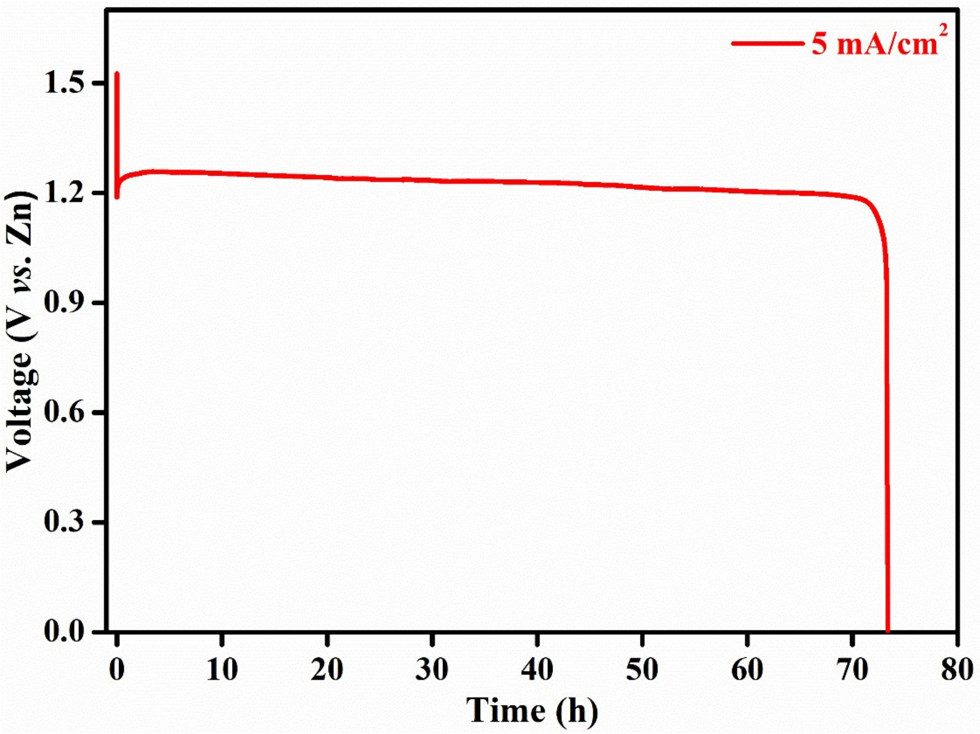

Figure S19. Galvanostatic charge-discharge plot of CoILPh 700 based zinc-air battery upon deep discharging at 5 mA/cm^2

Figure S20. Photograph of zinc anode after long charging the CoILPh 700 zinc-air battery at 5 mA/cm^2 for 72 h

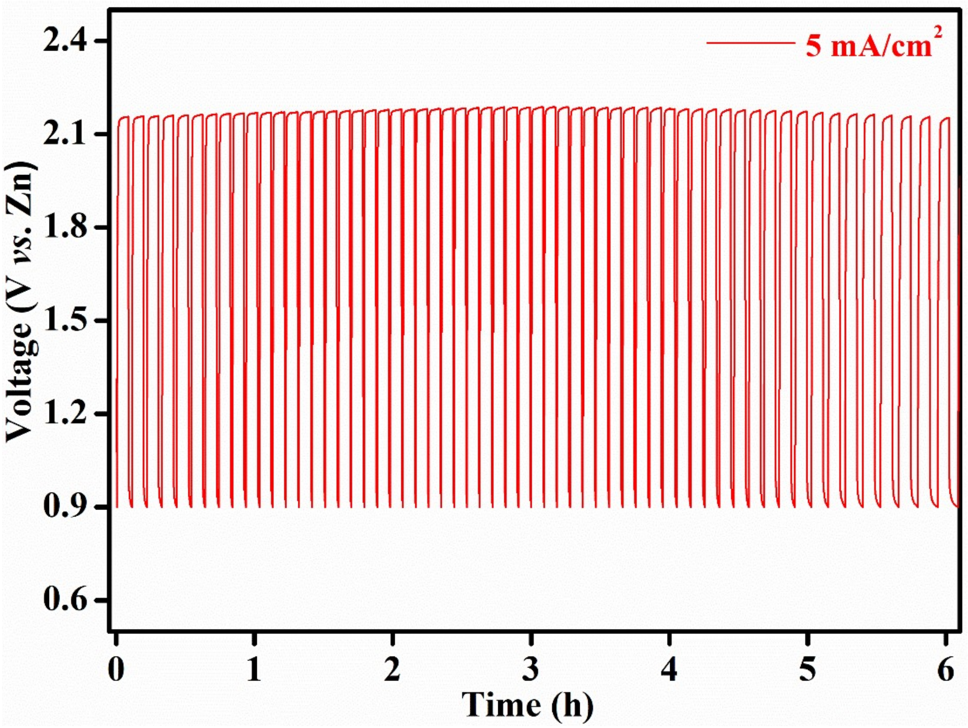

Figure S21. Galvanostatic charge-discharge plot of bare GDL-based zinc-air battery at 5 mA/cm^2

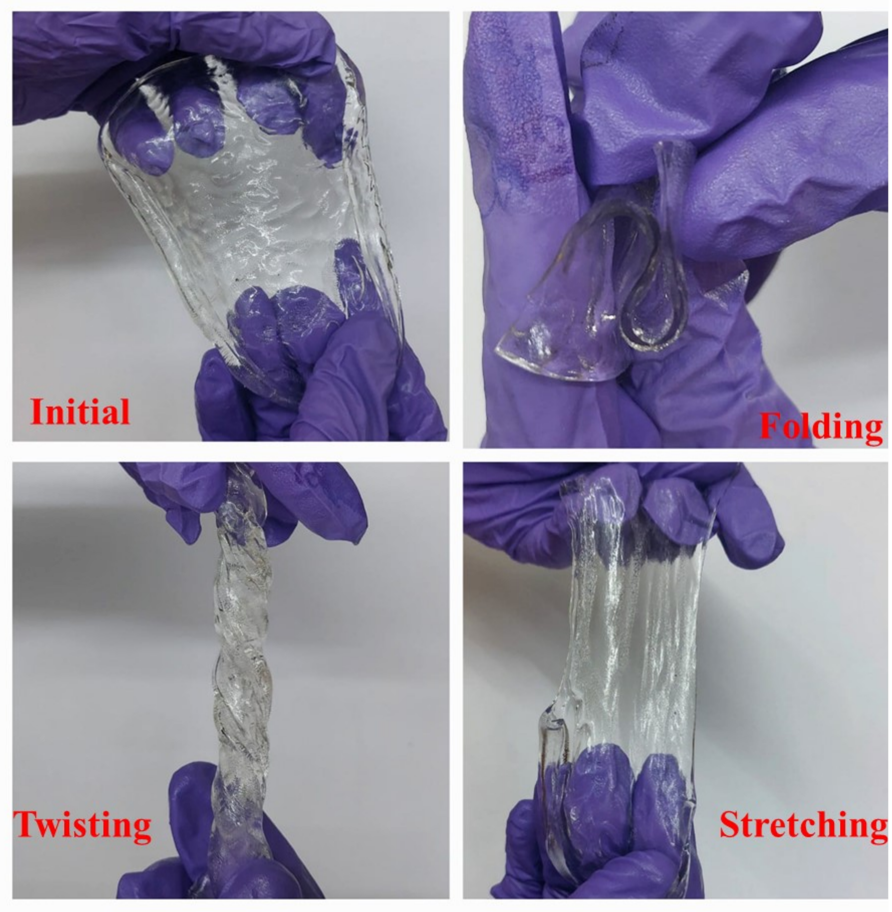

Figure S22. Images of PAM-based gel electrolyte upon various mechanical deformations of folding, twisting, and stretching

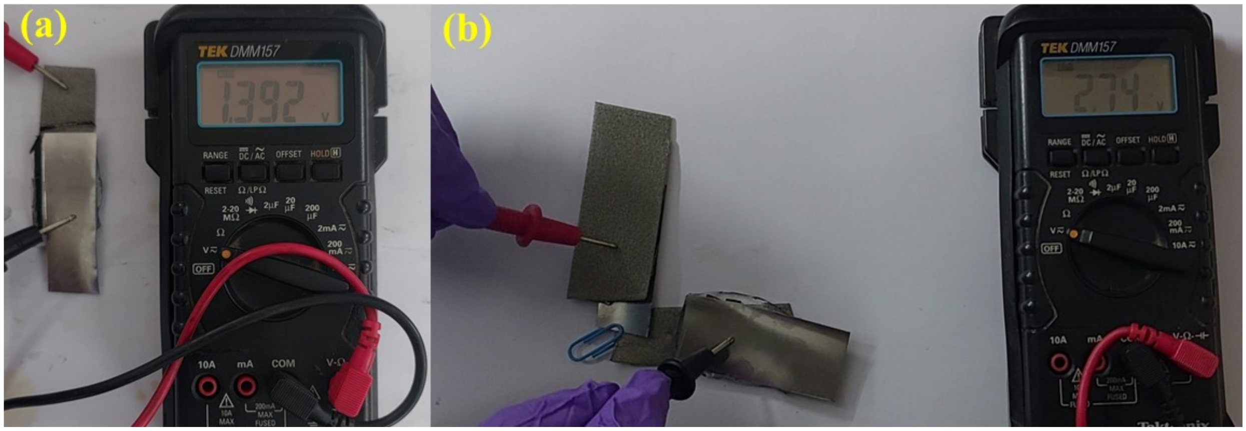

Figure S23. OCV of (a) assembled quasi solid-state zinc-air battery, and (b) series of two quasi solid-state zinc-air battery

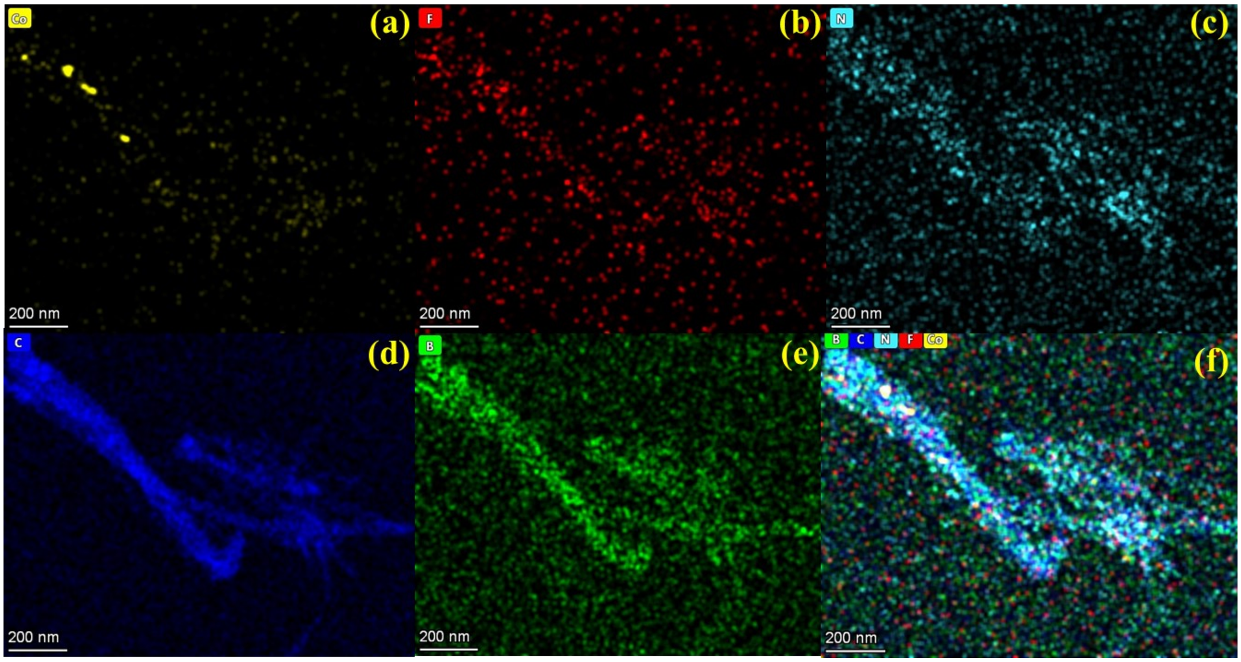

Figure S24. (a-f) HR-TEM elemental of CoILPh 700 post battery cycling at 5 mA/cm^2

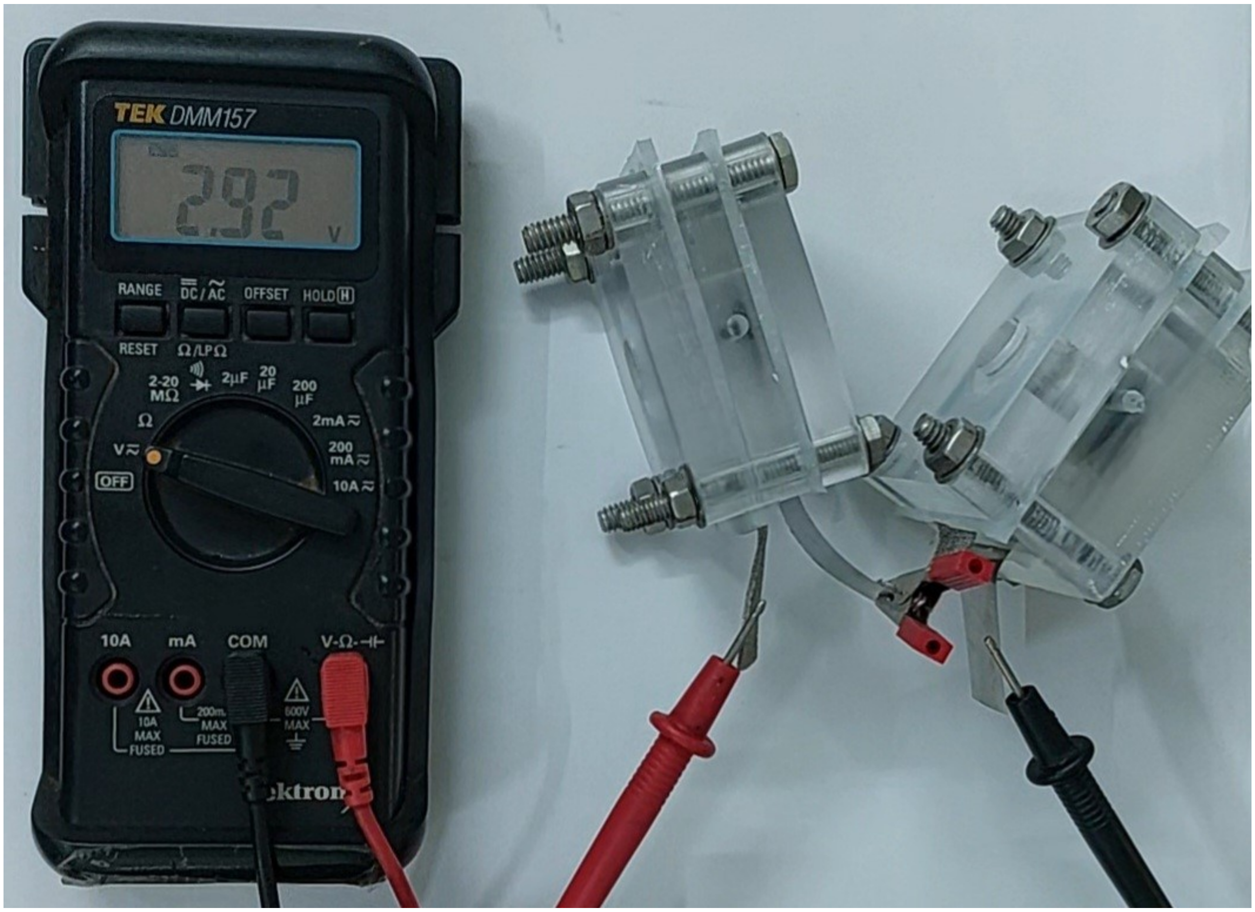

Figure S25. OCV of series of two liquid electrolyte CoILPh 700 based zinc-air battery

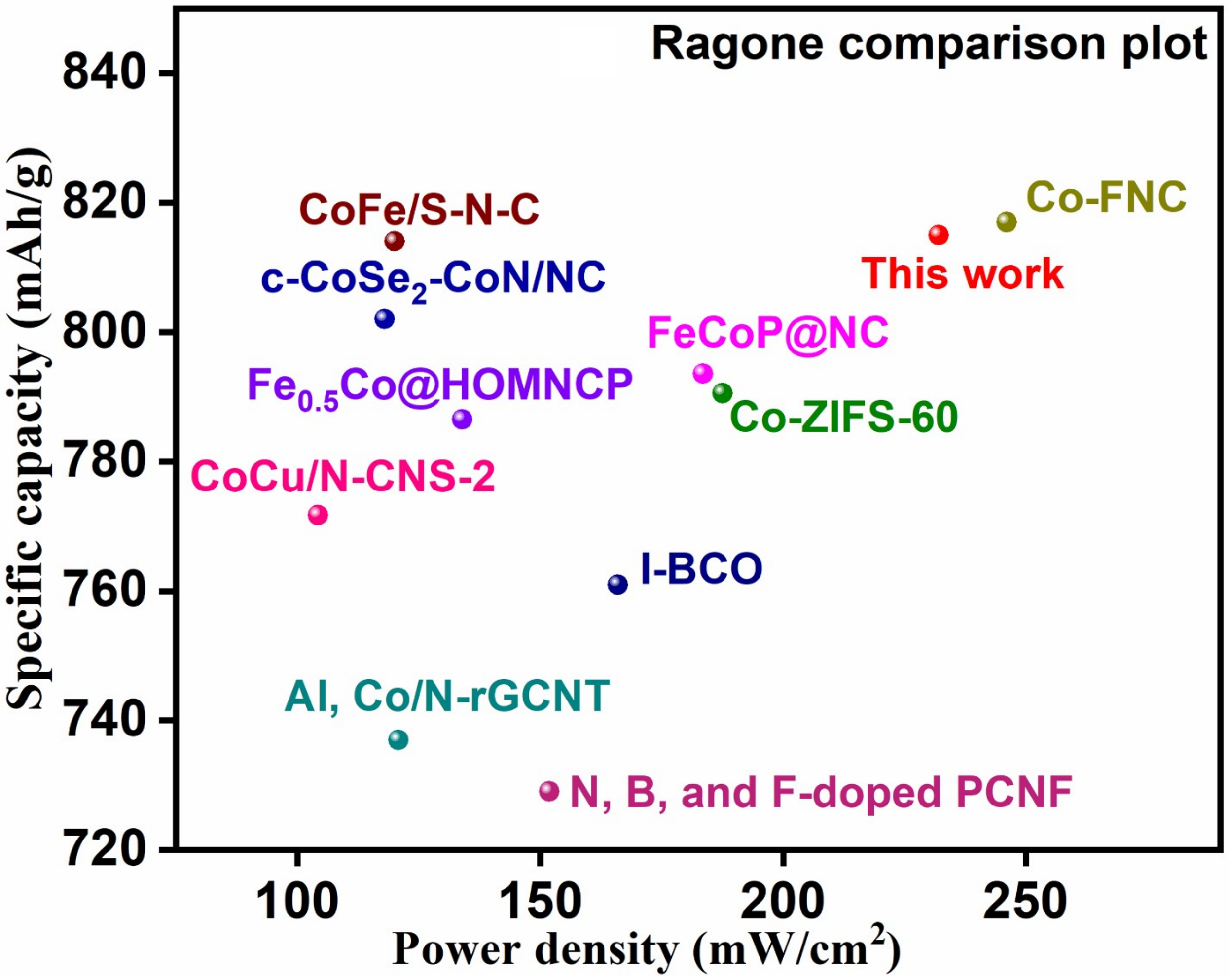

Figure S26. Ragone comparison plot of CoILPh 700 based zinc-air battery with recently published literature

In order to arrive at a Ragone plot, the power density value has been utilized from the polarisation profile. For the calculation of energy density from the deep discharge, we need to multiply the specific capacity in mAh/g with the average discharge voltage. The value of average discharge voltage being not available in literature, it would be an improper comparison to compare our energy density in Wh/kg with the literature specific capacity in mAh/g, henceforth we have utilized specific capacity values as such for comparison because specific capacity is directly proportional to the energy density.

Energy density (in Wh/kg) = Specific capacity (in mAh/g) × Average discharge voltage

Table S1. The surface content of elements in CoILPh 700, CoILPh 800, and CoILPh 900 from XPS

Materials	**Carbon**	**Nitrogen**	**Boron**	**Fluorine**	**Cobalt**
CoILPh 700	87.11	8.16	0.42	0.22	0.92
CoILPh 800	87.13	7.58	0.26	0.13	0.8
CoILPh 900	88.43	4.98	0.2	0.12	0.75

Table S2. The surface percentage of different types of nitrogen from XPS

Materials	**Surface % Nitrogen**	**Pyridinic-N**	**Co-Nx**	**Pyrrolic**	**Graphitic-N**
CoILPh 700	8.16	50.48	12.38	15.55	21.59
CoILPh 800	7.58	50.14	13.99	23.18	12.69
CoILPh 900	4.98	54.67	17.2	-	28.13

Table S3. The surface content of different types of cobalt from XPS

Materials	**Surface % Cobalt**	**Co^{2+} (Co-N)**	**Co^{3+} (Co-N)**	**Metallic Cobalt (Co-Co)**
CoILPh 700	0.92	35.13	28.77	9.31
CoILPh 800	0.8	35.45	26.44	11.72
CoILPh 900	0.75	43.49	24.22	16.93

Table S4. Comparison of the ORR activity of the synthesized catalyst with Pt/C in terms of onset potential (E_0), half wave potential ($E_{1/2}$), limiting current density (i_d) and Tafel slope

Materials	**Onset potential (V *vs.* RHE)**	**$E_{1/2}$ (V *vs.* RHE)**	**Limiting current density (mA/cm^2)**	**Tafel slope ($mV\ dec^{-1}$)**
CoIL 700	0.94	0.84	5.01	47
CoIL 800	0.933	0.79	4.36	57
CoIL 900	0.916	0.75	4.1	66
CoILPh 700	**0.956**	**0.85**	**5.68**	**45**
CoILPh 800	0.946	0.85	4.48	50
CoILPh 900	0.948	0.85	4.2	60
Pt / C	1.0	0.856	5.7	93

Table S5. The comparison of the OER activity of the synthesized catalyst with RuO_2 in terms of overpotential and Tafel slope

Materials	**Overpotential (mV *vs*. RHE)**	**Tafel slope (mV dec^{-1})**
CoIL 700	420	88
CoIL 800	422	92
CoIL 900	430	115
CoILPh 700	**380**	**63**
CoILPh 800	390	90
CoILPh 900	415	106
RuO_2	350	61

Table S6. The bifunctionality index of the synthesized electrocatalyst calculated from the difference of the OER overpotential and ORR halfwave potential

Bifunctionality index = OER potential (V) at J = 10 mA/cm² – ORR half wave potential (V)

Materials	**OER potential (V *vs.* RHE) at J = 10 mA/cm²**	**ORR $E_{1/2}$ (V *vs.* RHE)**	**Bifunctionality index (V)**
CoIL 700	1.65	0.84	0.81
CoIL 800	1.652	0.79	0.862
CoIL 900	1.66	0.75	0.91
CoILPh 700	**1.618**	**0.85**	**0.768**
CoILPh 800	1.62	0.85	0.77
CoILPh 900	1.645	0.85	0.795
Pt/C (20 %)	−	0.856	−
RuO_2	350	−	−

Table S7. The comparison of electrocatalytic performance in recent literature in terms of ORR onset potential, half-wave potential, limiting current density, and OER overpotential

Recent literatures	**ORR onset potential (V vs. RHE)**	**ORR $E_{1/2}$ (V vs. RHE)**	**ORR Limiting current density (mA/cm^2)**	**OER overpotential (mV *vs.* RHE)**	**References**
Co-S@NC	0.92	0.85	4.4	550	[1]
Co@NPCL	0.9	0.86	5.0	276	[2]
C-SDB-Co	1.0	0.95	4.4	-	[3]
CoOx@NHCS-800	0.95	0.86	5.25	-	[4]
Co-ZIF1.5/10CNF2	0.93	0.85	3.6	390	[5]
CoOx@NC-800	0.91	0.89	5.18	360	[6]
Co@NC-800	0.92	0.82	4.5	350	[7]
Co–N/C fiber	1.0	0.89	4.2	390	[8]
Co_2P/Co-NC	1.0	0.88	5.24	369	[9]
CoO@NC	0.86	0.82	5.54	326	[10]
Sp-Co_3O_4/C	0.88	0.75	6.6	380	[11]
CoP@PCNFs	0.95	0.81	5.0	250	[12]
CoILPh 700	**0.956**	**0.85**	**5.68**	**380**	**This work**

Table S8. The comparison of performance of aqueous rechargeable zinc-air battery in recent literature in terms of OCV, peak power density, specific capacity, time per cycle, and cycling stability

Recent literatures	Open circuit potential (V)	Peak power density (mW/cm^2)	Specific capacity (mAh/g$_{Zn}$)	Time per cycle (h)	Cycling stability @ Current density (mA/cm^2)	References
CoFe/S-N-C	1.479	120	814	0.33	100 @ 10	13
Fe$_{0.5}$Co@HOMNCP	1.619	134	786.5	-	120 @ 2	14
O–Co–N/C	1.47	143	785	-	150 @ 2	15
CoCu/N-CNS-2	1.424	104.3	771.7	0.16	400 @ 10	16
c-CoSe$_2$-CoN/NC	1.52	118	802	0.33	250 @ 10	17
FeCoP@NC	1.56	183.5	793.6	0.33	150 @ 1	18
Co-ZIF$_S$-60	-	187.5	790.57	0.16	160 @ 10	19
Co-FNC	1.55	246	817	0.5	300 @ 10	20
N, B, and F-doped PCNF	1.453	151.9	729	0.2	200 @ 5	21
Al, Co/N-rGCNT	1.35	120.8	737	0.16	193 @ 5	22
PPcCo/3D-G	1.410	347	776	0.16	350 @ 10	23
FeCo-NC800W	1.42	51.93	-	0.2	147 @ 5	24
CoFe@NCNT	1.49	194	795	0.33	299 @ 5	25
CoP-NC@NFP	1.44	93	-	0.66	200 @ 2	26
I-BCO	1.42	166	761	0.16	250 @ 2	27
CoILPh 700	**1.451**	**232**	**815**	**0.33** **2** **4**	**205 @ 5;** **296 @ 5;** **289 @ 5;**	

6	**140 @ 5;**	**This work**
8	**100 @ 5;**	
10	**62 @ 5;**	
144	**144 @ 5**	

References

1 N. Meng, Y. Feng, Z. Zhao and F. Lian, *Small*, 2024, **20**, 2400855.

2 T. Gu, J. Shen, Z. Sun, F. Li, C. Zhi, M. Zhu and J. Liu, *Small*, 2024, **20**, 2308355.

3 L. Fan, X. Dai, F. Li, X. Li, Z. Liu, Q. Guo, C. Zhang, Z. Kang and D. Sun, *J Mater Sci Technol*, 2025, **226**, 1–11.

4 C. Liu, S. Tuo, F. Wang and H. Zhu, *Electrochim Acta*, 2025, **513**, 145514.

5 H. He, Y. Lei, S. Liu, K. Thummavichai, Y. Zhu and N. Wang, *J Colloid Interface Sci*, 2023, **630**, 140–149.

6 M. Li, Q. Yang, L. Fan, X. Dai, Z. Kang, R. Wang and D. Sun, *ACS Appl Mater Interfaces*, 2023, **15**, 39448–39460.

7 H. Zheng, L. Lin, Z. Chen, T.-C. Yang, H. Wang, Z. Jiang, C. Bao, C.-M. Yang and N.-C. Lai, *J Colloid Interface Sci*, 2025, **686**, 624–633.

8 Y. Irmawati, F. Balqis, F. Destyorini, C. G. Adios, R. Yudianti, F. Iskandar and A. Sumboja, *ACS Appl Nano Mater*, 2023, **6(4)**, 2708-2718.

9 X. Liu, J. Wu, Z. Luo, P. Liu, Y. Tian, X. Wang and H. Li, *ACS Appl Mater Interfaces*, 2023, **15**, 9240–9249.

10 M. Chen, S. Han, M. Sun, J. Huang, Z. Li, Y. Xu, G. Cheng and L. Yu, *J Alloys Compd*, 2024, **971**, 172511.

11 B. Chutia, R. Chetry, K. N. Rao, N. Singh, P. Sudarsanam and P. Bharali, *ACS Appl Nano Mater*, 2024, **7**, 3620–3630.

12 N. Deng, Q. Zeng, Y. Feng, H. Gao, G. Wang, J. Yan, T. Zheng, Y. Liu, W. Kang and B. Cheng, *Catal Sci Technol*, 2023, **13**, 4823–4838.

13 G. Li, Y. Tang, T. Fu, Y. Xiang, Z. Xiong, Y. Si, C. Guo and Z. Jiang, *Chemical Engineering Journal*, 2022, **429**, 132174.

14 W. Li, B. Liu, D. Liu, P. Guo, J. Liu, R. Wang, Y. Guo, X. Tu, H. Pan, D. Sun, F. Fang and R. Wu, *Advanced Materials*, 2022, **34(17)**, 2109605.

15 W. Zhang, C. H. Xu, H. Zheng, R. Li and K. Zhou, *Adv Funct Mater*, DOI:10.1002/adfm.202200763.

16 J. Kuang, Y. Shen, Y. Zhang, J. Yao, J. Du, S. Yang, S. Zhang, Y. Fang and X. Cai, *Small*, DOI:10.1002/smll.202207413.

17 X. Xu, X. Wang, S. Huo, X. Liu, X. Ma, M. Liu and J. Zou, *Advanced Materials*, 2024, **36**, 2306844.

18 K. Muuli, R. Kumar, M. Mooste, V. Gudkova, A. Treshchalov, H.-M. Piirsoo, A. Kikas, J. Aruväli, V. Kisand, A. Tamm, A. Krumme, P. Moni, M. Wilhelm and K. Tammeveski, *Materials*, 2023, **16**, 4626.

19 C. Chen, Z. Chen, J. Zhong, X. Song, D. Chen, S. Liu, W.-C. Cheong, J. Li, X. Tan, C. He, J. Zhang, D. Liu, Q. Yuan, C. Chen, Q. Peng and Y. Li, *Nano Res*, 2023, **16**, 4211–4218.

20 D. Cao, Y. Mu, L. Liu, Z. Mou, S. Chen, W. Yan, H. Zhou, T.-S. Chan, L.-Y. Chang, L. Song, H.-J. Zhai and X. Fan, *ACS Nano*, 2024, **18**, 11474–11486.

21 A. Muthurasu, I. Pathak, D. Acharya, Y. R. Rosyara and H. Y. Kim, *J Mater Chem A Mater*, 2024, **12**, 1826–1839.

22 G. P. Kharabe, S. Barik, S. K. Veeranmaril, A. Nair, R. Illathvalappil, A. Yoyakki, K. Joshi, C. P. Vinod and S. Kurungot, *Small*, 2024, **2400012**, 1–15.

23 S. Wang, P. Sun, N. Li, J. Wang, L. Zhang, W. Duan and Z. Li, *J Power Sources*, 2023, **556**, 232471.

24 M. Etesami, R. Khezri, S. R. Motlagh, M. Gopalakrishnan, P. Mano, S. Namuangruk, S. Wannapaiboon, T. Yonezawa, A. Somwangthanaroj and S. Kheawhom, *Mater Today Energy*, 2024, 101649.

25 M. Wang, B. Liu, H. Zhang, Z. Lu, J. Xie and Y. Cao, *J Colloid Interface Sci*, 2024, **661**, 681–689.

26 E. Vijayakumar, S. Ramakrishnan, C. Sathiskumar, D. J. Yoo, J. Balamurugan, H. S. Noh, D. Kwon, Y. H. Kim and H. Lee, *Chemical Engineering Journal*, 2022, **428**, 131115.

27 D. Huang, T. Liu, A. Xu, J. Zhou, Y. Wang and X. Hu, *Electrochim Acta*, 2024, **494**, 144450.